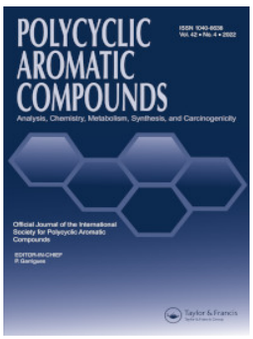

Polycyclic Aromatic Compounds

ISSN: (Print) (Online) Journal homepage: https://www.tandfonline.com/loi/gpol20

Spectroscopic, Solvent Effect, Molecular Docking and Molecular Dynamics Investigations on Phytocompounds from *Elettaria cardamomum* against Covid-19

R. Sangeetha, R. Premkumar, S. S. Maithili, C. Kirubhanand, S. Gowtham Kumar, P. Sangavi & K. Langeswaran

To cite this article: R. Sangeetha, R. Premkumar, S. S. Maithili, C. Kirubhanand, S. Gowtham Kumar, P. Sangavi & K. Langeswaran (2022): Spectroscopic, Solvent Effect, Molecular Docking and Molecular Dynamics Investigations on Phytocompounds from *Elettaria cardamomum* against Covid-19, Polycyclic Aromatic Compounds, DOI: 10.1080/10406638.2022.2086270

To link to this article: https://doi.org/10.1080/10406638.2022.2086270

Published online: 14 Jun 2022.

POLYCYCLIC AROMATIC COMPOUNDS
https://doi.org/10.1080/10406638.2022.2086270

Taylor & Francis
Taylor & Francis Group

Spectroscopic, Solvent Effect, Molecular Docking and Molecular Dynamics Investigations on Phytocompounds from *Elettaria cardamomum* against Covid-19

R. Sangeetha[a], R. Premkumar[b]*, S. S. Maithili[c]*, C. Kirubhanand[d], S. Gowtham Kumar[e], P. Sangavi[f], and K. Langeswaran[f]

[a]Department of Physics, Mannar Thirumalai Naicker College, Madurai, Tamil Nadu, India; [b]PG and Research Department of Physics, N.M.S.S.V.N. College, Madurai, Tamil Nadu, India; [c]AVS College of Arts & Science, Salem, Tamil Nadu, India; [d]Department of Anatomy, All India Institute of Medical Sciences, Nagpur, Maharashtra, India; [e]Faculty of Allied Health Sciences, Chettinad Hospital & Research Institute, Chettinad Academy of Research and Education (Deemed to Be University), Kelambakkam, Tamil Nadu, India; [f]Cancer Informatics Laboratory, Department of Bioinformatics, Alagappa University, Karaikudi, Tamil Nadu, India

ABSTRACT

To date, the globe has seen the many manifestations of Coronavirus. Outbreaks of various mutant strains of Coronavirus have been a severe threat to people, health, and medical sectors since its inception; this zoonotic virus has a fatality rate of about 50 lakhs with positive reports ranging from 24.5 cores to 24.5 cores. Recent advances in biomedical engineering and computational technology have provided us with a toolset of previously unimaginable possibilities for allowing transdisciplinary breakthroughs and highly rapid discoveries. Although approved vaccinations and treatments are extensively used to battle this dangerous virus, several additional medications are still required to cure or treat the various strains of Covid 19. Medicinal plants are high in anti-oxidants, anti-inflammatory properties, and anti-viral properties, among other things. The bioactive components from traditional medicinal plants and shrubs are treated to SARS-CoV variants such as Angiotensin-converting enzyme 2 (ACE2), Main protease (Mpro), Papain-like protease (PLpro), and Spike protein in this computational study. Furthermore, the lead complexes had higher docking values and better interactions with the target receptor's SARS-CoV binding sites. Throughout the simulation duration of roughly 50 ns, the lead complexes demonstrated greater affinity and stability. All of the Phytocompounds' pharmacological features were observed, including Human Oral Absorption, Molecular Weight, Blood-Brain Barrier, Hydrogen Bond Donor and Acceptor, and so on. Finally, the researchers found that the Docking and Dynamics analyses of the target receptors with the lead phytocompound from *Elettaria cardamomum* revealed possible inhibitory effects.

ARTICLE HISTORY
Received 8 February 2022
Accepted 24 May 2022

KEYWORDS
SARS-CoV; *Elettaria cardamomum*; Triprolidine; vibrational analysis; UV-Vis; molecular docking; molecular dynamics simulation

CONTACT C. Kirubhanand kirubhanand.c@gmail.com Department of Anatomy, All India Institute of Medical Sciences, Nagpur, Maharashtra, India; K. Langeswaran dr.langeswaran@gmail.com Cancer Informatics Laboratory, Department of Bioinformatics, Alagappa University, Science Campus, Karaikudi 630 003, India
*Equally contributed.

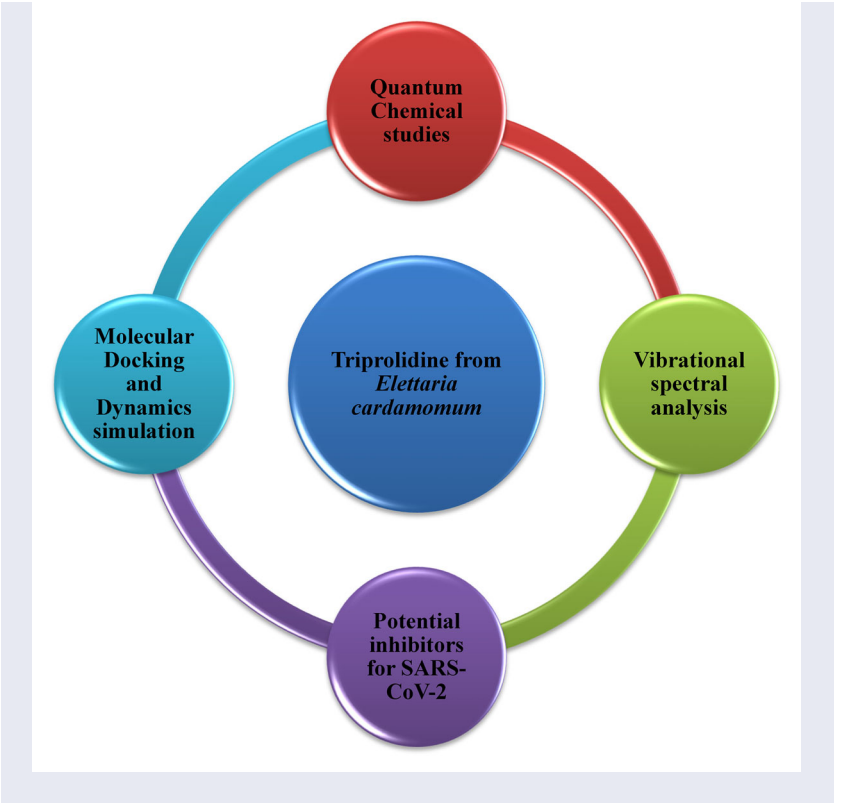

1. Introduction

The COVID-19 epidemic is today's most serious global health crisis and the universe's most serious concern. The Nidovirales order has three families: Roniviridae, Arteriviridae, and Coronaviridae.[1] Coronaviruses are members of the Coronaviridae family of viruses that infect wildlife and people. Coronaviruses are single-stranded, encapsulated RNA viruses with sizes ranging from 120 to 80 nm that fall into four categories: Alpha coronaviruses, Beta coronaviruses, Gamma coronaviruses, and Delta coronaviruses.[2] Coronaviruses, which have a crown-like appearance and afflict people of all ages, maybe spotted under an electron microscope. The illness is disseminated by large droplets produced by coughing and sneezing in infected persons. As a result, COVID-19's cumulative incidence varies by country, and instances have been confirmed on nearly every continent. The incubation period might last anywhere from 2 to 14 days. In some situations, increasing aerosol concentrations might lead to the spread of disease in confined spaces.[3] In settings with significant viral contamination, such as an infected person's house, environmental contamination is more likely to be a source of infection. COVID-19 can be transmitted in many ways, making it necessary for people to be aware of it at all times to stay safe. Asymptomatic to acute respiratory distress syndrome, septic shock, and multi-organ failure are among the clinical symptoms of this illness. The severity of this disease is best characterized, with mild, moderate, severe, and critical being the most common.

Elettaria cardamomum is a pungent, aromatic, herbaceous perennial plant known as the 'queen of spices,' light green or green cardamom, and little or lesser cardamom is widely recognized for its unique perfume and flavor. It has been used in medicine and cuisine for centuries. It was one of the most significant medicinal spices exchanged across civilizations, passing through western

Asia (the Middle East) on its way to Ancient Egypt, Greece, and Rome. This fragrant spice's traditional therapeutic benefits have been recorded in ancient Vedic texts reaching back 3000 years. Its anti-cholesterol and anticoagulant characteristics and its effect on multiple myeloma, blood pressure, vasodilation, and collective cardiac problems have all been described in studies.[4] It can be used to treat colds, coughs, asthma, bronchitis, TB, and sore throats, among other respiratory problems.[5] The presence of volatile oils and various bio-actives such as phenolics, 1,8-cineole, limonene, linalool, terpinolene, and myrcene is primarily responsible for the spice's historic therapeutic usage.[6] Computational techniques have been a cornerstone for novel drug development approaches and have acted as a crucial tool in drug discovery efforts. Computational techniques are used in practically every current drug development attempt, and computer-aided lead creation and optimization have had a lot of success. These methods are often precise, quick, and cost-effective. CADD refers to the more recent use of digital tools in the development of lead candidate designs.[7] At this juncture, the goal of this study is to examine the biophysical features of Triprolidine (Compound ID: 5282443) from *Elettaria cardamomum* and analyze its therapeutic potential against Covid-19 *in silico* approach.

2. Methodology – Computational details

2.1. Quantum chemical calculations

The global minimum energy molecular structure Triprolidine molecule was optimized by the DFT/B3LYP[8] method with cc-pVTZ basis set[9] using Gaussian 09 program.[10] The vibrational wavenumbers of the molecule were calculated and assigned based on PED calculations using the VEDA 4.0 program. The Gauss View 05[11] visualization tool was used to display the molecular structure, frontier molecular orbitals (FMOs), and molecular electrostatic potential (MEP) surface of the investigated molecule. Mulliken atomic charge values were obtained using Mulliken population analysis using the 6–31 G (d,p) basis set. All DFT calculations were performed at the Triprolidine (Compound ID: 5282443) molecule's ground state energy level, with no constraints on the potential energy surface.

2.2. Molecular docking

2.2.1. Identifying the target

Protein structures acquired from Protein Data Bank. In the protein preparation wizard, the protein structure is imported into Maestro.[12] Consequently, the structure was reduced to its bare minimum and optimized. Structure minimization has been used to improve the structure using restricted minimization.[13]

2.2.2. Preparation of ligand

The selected bioactive chemicals were identified as a Ligand using GC-MS analysis. Ligand structure preparation is intended to generate high-quality, all-atom 3D structures for many druggable compounds, beginning with a 2D or 3D in SDF or Maestro format.

2.2.3. Receptor grid generation

The Grid was built utilizing Receptor Grid generation. Ligand docking is not possible without the Grid box. It was necessary to have a constructed target structure with the proper order of bond and formal alterations to produce a Grid.

2.2.4. Glide

Gliding-based docking (Glide) is the docking strategy in the Schrodinger suite. Glide was employed as a filter to find the ligand position in the active site. The highest scored ligands of the relevant protein model were docked using XP docking.

2.2.5. Screening

For Ligand and Receptor docking, the Glide module is used in this workflow. In three different modes, glide screens the molecules: High Throughput Virtual Screening (HTVS), Standard Precision (SP), and Extra Precision (XP). Compounds with the highest score of Glide and its energy were visually evaluated and selected for more investigation.

2.2.6. Molecular docking

Docking was carried out using Glide's XP, one of the modules (Schrodinger, 2015), Ligand docking with five taps. Dock flexibility is a configurable option in Glide that confirms the docking procedure.[14] Glide XP visualization was used to show docking scores and 3D visualization for the XP.

2.2.7. Binding free energy

The binding energy between the target and the collection of ligands was calculated using Prime/MM-GBSA.[15] Using the (OPLS-AA) 2005 force field and the GB/SA solvent model, Protein-Ligand binding energy was calculated.

2.2.8. Prediction of ADMET property

Compound efficiency and safety are crucial variables to disclose in the market; these factors may be assessed utilizing an Absorption, Distribution, Metabolism, Excretion, and Toxicity profile. The identified chemical is deemed a drug-like molecule that satisfies pharmaceutical relevant requirements. QikProp module was used to evaluate the pharmacological properties.[16]

2.2.9. Pharmacophore features

Ligand-based and structure-based have come under the Pharmacophores methods employed to yield energy-optimized, structure-based pharmacophores that can be used in compounds to screen in millions. The pharmacophore hypothesis generated pharmacophoric features of the input ligands.

2.2.10. Simulation of molecular dynamics (MDS)

Water molecules were included in MD simulations to test the complex's stability through the docking approach. MDS was acknowledged circumstances closer to the physiological environment, revealing improved binding confirmations for docked complexes.[17] The Root Mean Square Deviation was calculated for each complex to assess protein stability and conformation changes during 50 ns. Furthermore, the complex's RMSF (Root Mean Square Fluctuation) was examined; it is critical to comprehend complexes' interaction throughout the 50 ns for inhibitory processes. An MD simulation was performed to test the Protein-Ligand complexes' stability. The RMSD value is used to assess protein stability. GROMACS 4.6.1 was used to examine the dynamic behavior of the complex.[18] For the complex, MD was performed at 50 ns. The structure's coordinates were saved and evaluated using the systematic tool included in the GROMACS 4.6.1 package.

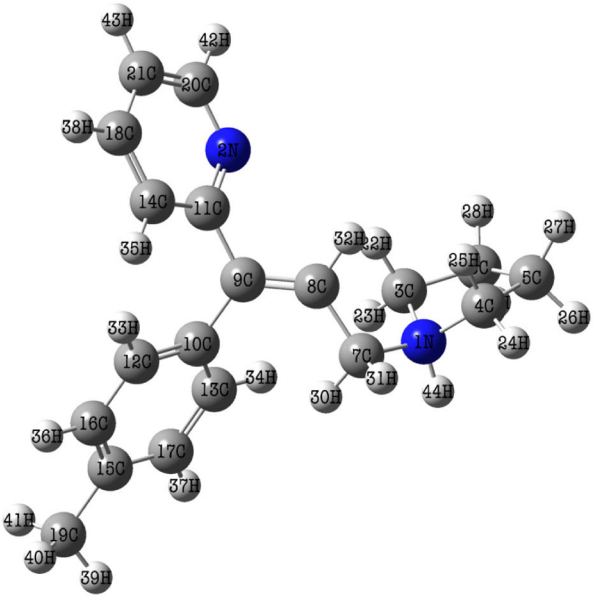

Figure 1. The optimized molecular structure of Triprolidine.

3. Results and discussion

3.1. Molecular geometry analysis

The DFT/B3LYP method optimized the title molecular structure using the cc-pVTZ basis set.[19] The cc-pVTZ basis set computed the energy values of the optimized molecular geometry as 847.39 a.u. Figure 1 depicts the optimized molecular structure of the Triprolidine (Compound ID: 5282443) molecule.

Table 1 shows the calculated structural properties of the molecule, such as bond length, bond angle, and dihedral angle values. The molecular geometry of the Triprolidine (Compound ID: 5282443) molecule possesses C_1 point group symmetry. The molecule's vibrational modes are all IR and Raman active, implying that the Triprolidine molecule has a non-centrosymmetric structure. The optimized molecular geometry of the Triprolidine molecule is located at a local minimum on the potential energy surface, as evidenced by the absence of negative vibrational wavenumbers.[20]

3.2. Vibrational spectral analysis

The compound Triprolidine has 44 atoms and 126 normal vibrations modes, which belong to the same symmetry species. For the most stable optimized structure of the Triprolidine molecule, the vibrational frequencies, IR intensity, and Raman scattering activity were calculated, which were shown in Table 2. The chemical Triprolidine has C1 point group symmetry, with no other symmetry beyond identity. The normal modes of vibrations belong to the symmetry species (A). Figure 2 depicts the molecule's theoretically simulated infrared and Raman spectra. The theoretically calculated vibrational wavenumbers values were correlated well with the available experimental vibrational wavenumbers,[21–28] which are also assigned based on PED calculations. The molecule's vibrational functions were calculated using the VEDA 4.0 programme, which several researchers have recognized as a valuable tool for determining vibrational frequencies.[29]

Table 1. The optimized structural parameters of the Triprolidine molecule were calculated by the DFT/B3LYP method with a cc-pVTZ basis set.

Structural parameters	cc-pVTZ	Structural parameters	cc-pVTZ
Bond length (Å)			
N1-C3	1.47	C9-C10	1.48
N1-C4	1.47	C9-C11	1.46
N1-C7	1.49	C10-C12	1.41
N1-H44	1.02	C10-C13	1.41
N2-C11	1.36	C11-C14	1.42
N2-C20	1.33	C12-H33	1.09
C3-C6	1.08	C13-C17	1.39
C3-H22	1.39	C13-H34	1.09
C3-H23	1.09	C14-H35	1.08
C4-C5	1.56	C15-C16	1.40
C4-H24	1.09	C15-C17	1.40
C5-H25	1.09	C15-C19	1.51
C5-C6	1.56	C16-H36	1.09
C5-H26	1.09	C17-H37	1.09
C5-H27	1.09	C18-C21	1.39
C6-H28	1.10	C18-H38	1.09
C6-H29	1.10	C19-H39	1.09
C7-C8	1.37	C19-H40	1.09
C7-H30	1.09	C19-H41	1.10
C7-H31	1.09	C20-C21	1.40
C8-C9	1.42	C20-H42	1.09
C8-H32	1.09	C21-H43	1.09
Bond angle (degree)			
C3-N1-C4	104.26	N1-C4-C5	107.09
C3-N1-C7	103.08	N1-C4-H24	110.48
C3-N1-H44	109.22	N1-C4-H25	107.97
C4-N1-C7	103.22	C5-C4-H24	113.57
C4-N1-H44	109.32	C5-C4-H25	110.21
C7-N1-H44	125.71	H24-C4-H25	107.38
C11-N2-C20	118.86	C4-C5-C6	104.37
N1-C3-C6	106.83	C4-C5-H26	110.79
N1-C3-H22	107.99	C4-C5-H27	111.57
N1-C3-H23	110.56	C6-C5-H26	110.79
C6-C3-H22	110.17	C6-C5-H27	112.28
C6-C3-H23	113.65	H26-C5-H27	107.07
H22-C3-H23	107.48	C3-C6-C5	104.22
C3-C6-H28	111.94	C17-C13-H34	119.52
C3-C6-H29	110.40	C11-C14-C18	119.66
C5-C6-H28	112.50	C11-C14-H35	120.00
C5-C6-H29	110.67	C18-C14-H35	120.32
H28-C6-H29	107.12	C16-C15-C17	117.67
N1-C7-C8	123.23	C16-C15-C19	121.21
N1-C7-H30	114.23	C17-C15-C19	121.09
N1-C7-H31	8.58	C12-C16-C15	121.29
C8-C7-H30	121.76	C12-C16-H36	119.24
C8-C7-H31	120.64	C15-C16-H36	119.46
H30-C7-H31	117.57	C13-C17-C15	121.24
C7-C8-C9	126.80	C13-C17-H37	119.27
C7-C8-H32	118.14	C15-C17-H37	119.47
C9-C8-H32	115.03	C14-C18-H21	119.22
C8-C9-C10	120.80	C14-C18-H38	120.08
C8-C9-C11	119.44	H21-C18-H38	120.69
C10-C9-C11	119.75	C15-C19-H39	111.42
C9-C10-C12	121.24	C15-C19-H40	111.41
C9-C10-C13	121.24	C15-C19-H41	111.12
C12-C10-C13	117.50	H39-C19-H40	108.05
N2-C11-C9	117.50	H39-C19-H41	107.27
N2-C11-C14	120.53	H40-C19-H41	107.33
C9-C11-C14	121.94	N2-C20-C21	124.13
C10-C12-C16	121.11	N2-C20-H42	115.79

(*continued*)

Table 1. Continued.

Structural parameters	cc-pVTZ	Structural parameters	cc-pVTZ
C10-C12-H33	119.19	C21-C20-H42	120.07
C16-C12-H33	119.68	C18-C21-C20	117.57
C10-C13-C17	121.16	C18-C21-H43	121.79
C10-C13-H34	119.30	C20-C21-H43	120.62
Dihedral angle (degree			
C4-N-C3-C6	36.28	C3-N1-C4-H24	−158.95
C4-N1-C3-H22	−82.21	C3-N1-C4-H25	83.88
C4-N1-C3-H23	160.43	C7-N1-C4-C5	−142.23
C7-N1-C3-C6	143.82	C7-N1-C4-H24	93.60
C7-N1-C3-H22	25.32	C7-N1-C4-H25	−23.55
C7-N1-C3-H23	−92.02	H44-N1-C4-C5	81.89
H44-N1-C3-C6	−80.47	H44-N1-C4-H24	−42.26
H44-N1-C3-H22	161.02	H44-N1-C4-H25	−159.42
H44-N1-C3-H23	43.67	C3-N1-C7-C8	−159.26
C3-N1-C4-C5	−34.79	C3-N1-C7-H30	10.88
C3-N1-C7-H31	125.68	N1-C7-C8-H32	−7.72
C4-N1-C7-C8	−50.94	H30-C7-C8-C9	1.14
C4-N1-C7-H30	119.20	H30-C7-C8-H32	−177.15
C4-N1-C7-H31	−125.99	H31-C7-C8-C9	−179.78
H44-N1-C7-C8	75.03	H31-C7-C8-H32	1.92
H44-N1-C7-H30	−114.81	C7-C8-C9-C10	6.31
H44-N1-C7-H31	−0.01	C7-C8-C9-C11	−173.78
C20-N2-C11-C9	−179.24	H32-C8-C9-C10	−175.34
C20-N2-C11-C14	−0.68	H32-C8-C9-C11	4.55
C11-N2-C20-C21	−0.05	C8-C9-C10-C12	57.24
C11-N2-C20-H42	−179.90	C8-C9-C10-C13	−121.76
N1-C3-C6-C5	−23.48	C11-C9-C10-C12	−122.64
N1-C3-C6-H28	−145.35	C11-C9-C10-C13	58.34
N1-C3-C6-H29	95.39	C8-C9-C11-N2	11.26
H22-C3-C6-C5	93.58	C8-C9-C11-C14	−167.27
H22-C3-C6-H28	−28.28	C10-C9-C11-N2	−168.83
H22-C3-C6-H29	−147.53	C10-C9-C11-C14	12.62
H23-C3-C6-C5	−145.71	C9-C10-C12-C16	−179.48
H23-C3-C6-H28	92.42	C9-C10-C12-H33	1.12
H23-C3-C6-H29	−26.83	C13-C10-C12-C16	−0.43
N1-C4-C5-C6	19.73	C13-C10-C12-H33	−179.82
N1-C4-C5-H26	−99.56	C9-C10-C13-C17	178.98
N1-C4-C5-H27	141.22	C9-C10-C13-H34	0.16
H24-C4-C5-C6	141.98	C12-C10-C13-C17	−0.05
H24-C4-C5-H26	22.68	C12-C10-C13-H34	−178.88
H24-C4-C5-H27	−96.52	N2-C11-C14-C18	0.79
H25-C4-C5-C6	−97.48	N2-C11-C14-H35	−178.15
H25-C4-C5-H26	143.21	C9-C11-C14-C18	179.28
H25-C4-C5-H27	24.01	C9-C11-C14-H35	0.33
C4-C5-C6-C3	2.19	C10-C12-C16-C15	0.42
C4-C5-C6-H28	123.69	C10-C12-C16-H36	−179.58
C4-C5-C6-H29	−116.50	H33-C12-C16-C15	179.81
H26-C5-C6-C3	121.49	H33-C12-C16-H36	−0.19
H26-C5-C6-H28	−117.01	C10-C13-C17-C15	0.58
H26-C5-C6-H29	2.79	C10-C13-C17-H37	−179.07
H27-C5-C6-C3	−118.82	H34-C13-C17-C15	179.40
H27-C5-C6-H28	2.66	H34-C13-C17-H37	−0.25
H27-C5-C6-H29	122.47	C11-C14-C18-C21	−0.16
N1-C7-C8-C9	170.56	C11-C14-C18-H38	−179.72
H35-C14-C18-C21	178.78	C16-C15-C19-H41	91.90
H35-C14-C18-H38	−0.77	C17-C15-C19-H39	32.60
C17-C15-C16-C12	0.09	C17-C15-C19-H40	153.38
C17-C15-C16-H36	−179.90	C17-C15-C19-H41	−86.97
C19-C15-C16-C12	−178.81	C14-C18-C21-C20	−0.52
C19-C15-C16-H36	1.18	C14-C18-C21-H43	179.84
C16-C15-C17-C13	−0.59	H38-C18-C21-C20	179.03
C16-C15-C17-H37	179.06	H38-C18-C21-H43	−0.60

(*continued*)

Table 1. Continued.

Structural parameters	cc-pVTZ	Structural parameters	cc-pVTZ
C19-C15-C17-C13	178.32	N2-C20-C21-C18	0.66
C19-C15-C17-H37	−2.02	N2-C20-C21-H43	−179.69
C16-C15-C19-H39	−148.51	H42-C20-C21-C18	−179.49
C16-C15-C19-H40	−27.74	H42-C20-C21-H43	0.14

3.3. Analysis of frontier molecular orbitals (FMOs)

FMOs are defined as the highest occupied molecular orbital (HOMO) and the lowest unoccupied molecular orbital (LUMO), which determine how a molecule interacts with other species. The HOMO energy denotes the ability to give electrons, while the LUMO energy denotes the ability to take electrons.[30] In addition to UV–Vis spectra and quantum chemistry, FMOs play a vital role in electric and optical properties.[31] The HOMO–LUMO gap aids in the explanation of the molecule's kinetic stability and chemical reactivity, both of which are essential parameters in determining its electronic properties. A small HOMO–LUMO gap molecule is a soft molecule because it has low kinetic stability and strong chemical reactivity. The molecule's FMOs were depicted in Figure 3, and the FMOs' relevant molecular characteristics were estimated using Koopman's theorem,[32] as shown in Table 3. The positive phase is red, whereas the negative phase is green, as illustrated in Figure 3. The calculated low energy gap value (2.53 eV) confirms the higher chemical reactivity of the Triprolidine molecule. It explains the intramolecular charge transfer interaction within the molecule, which influences its biological activity.[33] Ionization energy (I), $I = -E_{HOMO}$, is the energy required to remove an electron from a filled orbital. Electron affinity (A), $A = -E_{LUMO}$, is the energy released when an electron is added to an unfilled orbital. The molecule's calculated high ionization energy (7.26 eV) and low electron affinity (4.73 eV) indicate that electrophilic and nucleophilic attacks are both possible. The global hardness, $\eta = 1/2\ (E_{LUMO}-E_{HOMO})$; global softness, $S = 1/\eta$; electronic chemical potential, $\mu = 1/2\ (E_{LUMO} + E_{HOMO})$; and global electrophilicity index, $\psi = \mu^2/2\eta$ of the molecule were also calculated. The predicted values of higher hardness (1.27 eV) and lower softness (0.79 eV) imply that the molecule is stable. The molecule's predicted chemical potential (5.99 eV) and electrophilicity index (14.12 eV) confirm its chemical stability, equivalent to those of potentially bioactive compounds.[34]

3.4. Solvent effect on the UV-visible spectrum

The solvent effect on UV-Visible spectra and the corresponding electronic transitions of the Triprolidine molecule were predicted using the TD-DFT/CAM-B3LYP method with a cc-pVTZ basis set. The TD-DFT computation is an effective technique for studying molecules' static and dynamic characteristics in excited states.[35] Figure 4 depicts the simulated UV-Visible spectra of the Triprolidine (Compound ID: 5282443) molecule in the gas phase and several solvents including ethanol, methanol, water, DMSO, and Acetone. The calculated absorption wavelength (λ), excitation energies (E), and oscillator strength (f) for gas phase and various solvents are listed in Table 4.

As shown in Figure 4, the first peak for solvents was observed around 347 nm, while the corresponding peak in the gas phase was absent. The second peak in the gas phase and solvent was most intense, around 607 nm and 617 nm, respectively. As listed in Table 4, the obtained data results could be retrieved through the more considerable oscillator strength and absorptivities observed in solvents than in the gas phase. In conclusion, the solvent facilitates absorption with the highest oscillator strength in Acetone. Furthermore, an impressive bathochromic shift (redshift) of absorption maxima is observed when moving from the gas phase to the solvent phase. This is due to the dipole interaction between solvent molecules and the solute, which lowers the

Table 2. The calculated vibrational frequencies (cm^{-1}), IR intensities (Km mol^{-1}), Raman scattering activity ($Å^4$ amu^{-1}), and vibrational assignments based on PED calculations for the Triprolidine molecule.

ν_{cal}	[a]I IR	[b]I Raman	Assignment with PED%	ν_{cal}	[a]I IR	[b]I Raman	Assignment with PED%
3503	1.04	107.27	ν N-H (100)	3117	16.38	73.63	ν_{as} C-H_3 (100)
3238	20.60	213.46	ν_{as} C-H_2 (97)	3113	78.68	51.17	ν_{as} φ C-H_2 (81)
3226	5.02	105.40	ν Φ C-H (94)	3106	28.88	96.62	ν_{as} φ C-H_2 (74)
3209	12.22	264.04	ν Φ C-H (94)	3099	4.49	172.74	ν_{as} φ C-H_2 (89)
3201	5.33	107.49	ν ϕ C-H (89)	3089	19.38	104.72	ν_{as} C-H_3 (99)
3193	22.76	70.03	ν ϕ C-H (98)	3084	18.67	23.52	ν_{as} φ C-H_2 (88)
3192	4.94	58.04	ν C-H (96)	3060	59.44	256.66	ν_s φ C-H_2 (96)
3185	11.56	119.28	ν Φ C-H (95)	3047	28.37	56.51	ν_s φ C-H_2 (99)
3171	20.35	99.85	ν ϕ C-H (88)	3039	44.22	134.79	ν_s φ C-H_2 (93)
3169	15.54	100.56	ν ϕ C-H (97)	3032	35.58	61.53	ν φ C-H (85)
3155	36.68	170.29	ν Φ C-H (96)	3031	44.22	393.06	ν_s C-H_3 (100)
3137	33.87	394.74	ν_s C-H_2 (96)	1654	8.36	332.79	ϕ C-C (48)
1617	70.58	545.25	Φ C-N (10), Φ C-C (46), β Φ C-H (10)	1282	1.67	61.35	ν C=C (11) ν Φ C-N (29)
1601	1.46	13.45	ϕ C-C (52)	1279	0.11	2.14	ω φ C-H_2 (59)
1593	12.08	10.18	Φ C-N (10), Φ C-C (31), β Φ C-H (10)	1261	14.96	231.69	ν C=C (12) ν C-C (19) β C-H (18)
1562	1.34	98.41	δ C-H_2 (75)	1254	2.86	5.31	t φ C-H_2 (67)
1544	17.07	50.42	β ϕ C-H (55)	1234	3.03	27.26	ν C-C (41)
1523	1.23	3.95	δ φ C-H_2 (95)	1216	0.90	3.94	t φ C-H_2 (62)
1505	3.50	4.85	δ φ C-H_2 (84)	1213	4.16	4.46	β φ C-H (58)
1502	1.99	4.41	δ φ C-H_2 (85)	1211	3.51	21.89	β ϕ C-H (70)
1495	21.22	13.71	δ C-H_3 67)	1178	7.19	40.09	β ϕ C-H (76) ν ϕ C-C (10)
1493	3.85	13.79	δ C-H_3 67)	1150	3.38	65.32	ν C-C (15)
1492	19.85	14.29	ν Φ C-N (11) δ φ C-H_2 (84)	1141	5.08	1.15	β ϕ C-H (47) ν ϕ C-C (24)
1491	7.81	45.04	ν Φ C-N (11) δ φ C-H_2 (56)	1115	2.58	3.10	β Φ C-H (33) ν Φ C-C (26)
1460	14.47	7.34	β φ N-H (49)	1104	18.77	0.35	ν φ C-N (56) β φ CCN (20)
1457	48.24	65.09	β Φ C-H (43)	1073	2.27	51.27	β Φ C-H (21) ν Φ C-C (33)
1448	8.65	142.74	β C-H (28)	1061	10.78	0.29	β C-H_3 (77)
1433	2.02	31.98	ϕ C-C (28) β ϕ C-H (23)	1060	0.66	0.79	τ φ HNHC (15) τ φ CCNC (33)
1419	0.12	35.61	β C-H_3 (94)	1051	7.46	32.75	ν Φ C-C (10) β C-H (28) β Φ CNC (13)
1374	8.77	126.43	C-C (32) β Φ C-H (23)	1041	0.51	6.02	β φ CNC (13) β φ CCN (17)
1373	4.17	18.38	ω φ C-H_2 (55)	1036	2.92	0.52	β ϕ CCC (77)
1343	6.69	79.25	ν Φ C-N (10) β ϕ C-H (21)	1019	7.17	13.62	η C-H (77)
1341	0.23	2.61	ω φ C-H_2 (29)	1006	0.01	0.70	η C-H (61)
1339	6.38	63.98	ν Φ C-N (10)	1005	0.28	1.33	η Φ C-H (61)
1335	0.07	13.89	t φ C-H_2 (63)	992	7.72	141.49	β Φ ring (67)
1319	2.55	43.37	ν Φ C-N (13) ν Φ C-C (25)	985	0.14	1.79	η ϕ (88)
1311	0.14	0.55	ω φ C-H_2 (51)	979	0.33	1.04	η Φ (75)
1307	2.80	244.29	ν C-C (15) β Φ C-H (11)	977	14.26	17.17	ν φ C-C (11) β φ CCN (18) β φ HNH (11)
969	0.49	0.58	η ϕ (79)	624	0.79	1.24	t φ (12)
934	24.44	4.02	ν φ C-N (61)	619	13.45	7.07	Ring vibration
932	3.83	5.34	ring breathing	551	5.80	1.35	Φ C-H (27)
919	34.80	7.28	ω C-H_2 (54)	542	5.79	7.2	β Φ CCC (10)
917	14.34	4.28	ω C-H_2 (18)	481	1.70	0.83	τCCCC (14)
895	0.71	1.95	η Φ C-H (78)	448	2.25	2.86	τ Φ CCCN (20)
886	13.23	29.24	β φ CNC (31)	423	1.39	8.63	τ ϕ CCCC (75)

(*continued*)

Table 2. Continued.

ν_{cal}	[a]I IR	[b]I Raman	Assignment with PED%	ν_{cal}	[a]I IR	[b]I Raman	Assignment with PED%
856	1.36	13.57	η ϕ C-H (98)	413	3.03	5.97	τ ϕ CCCC (40)
849	1.68	0.67	ρ φ C-H_2 (25)	399	0.89	14.85	Ring vibration
836	24.75	0.49	η ϕ C-H (64)	351	0.86	1.79	t Ring
831	119.97	2.73	η φ N-H (70)	328	0.34	1.28	Lattice vibration
811	0.50	41.40	Φ Ring Breathing	293	1.73	3.66	t Ring
799	1.2	0.39	ρ φ C-H_2 49)	285	7.61	0.13	t φ C-H_2 (12)
798	25.05	7.49	η Φ C-H (63)	209	0.83	7.26	Lattice vibration
746	24.45	2.78	η Φ C-H (80)	205	0.62	4.71	Lattice vibration
736	5.51	2.06	η ϕ C-H (61)	185	0.66	3.69	Lattice vibration
707	3.52	2.62	Ring vibration	159	0.68	1.64	Lattice vibration
690	5.08	1.04	t C-H_2 (22)	105	1.35	3.68	Lattice vibration
652	0.81	4.62	β ϕ (59)	71	0.22	9.59	Lattice vibration
643	0.78	0.91	β φ CCN (48)	63	0.75	8.49	Lattice vibration
638	1.51	2.76	β Φ CCC (13) β Φ CCN (36)	52	0.80	2.97	Lattice vibration

ν – Stretching, ν_s – symmetrical stretching, ν_{as} – asymmetrical stretching, β – in-plane bending, δ –Scissoring, ρ – Rocking, ω – Wagging, τ – Torsion, η – Out of plane bending, Φ – Pyridine ring, ϕ – Benzene ring, φ – Pyrrolidine ring, ν_{cal} – calculated vibrational frequency, [a]I IR – Infrared spectra intensity, [b]I Raman – Raman scattering activities.

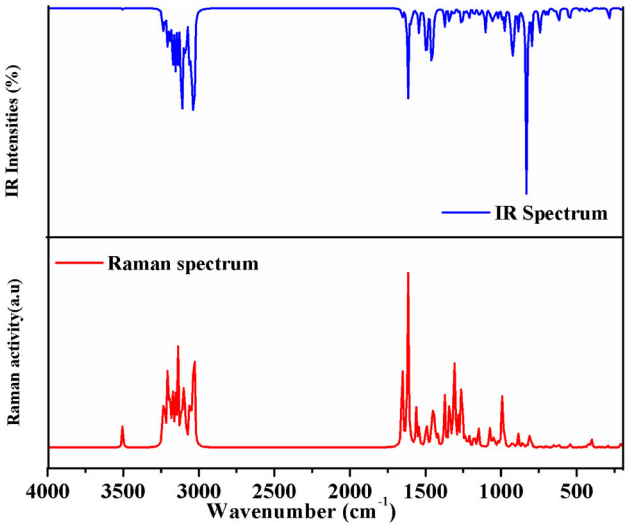

Figure 2. The simulated infrared and Raman spectra of Triprolidine.

energy of the excited state more than the ground state because excited states are more polar than the ground state.[35]

3.5. MEP surface analysis

The total electron density mapped with MEP surface analysis gives a visual representation of a molecule's chemically active regions and improves understanding of molecular reactivity, electrophilic reactions, substituent effects, intramolecular interactions, and so on.[36] The MEP surface of the Triprolidine is shown in Figure 5. The colors red, yellow, light blue, and blue on the MEP surface correspond to electron-rich, slightly electron-rich, slightly electron-deficient, and electron-deficient regions, respectively. Because of the lone pair of nitrogen atoms, the region around the nitrogen atom N2 was electron-rich (red). Furthermore, in the title molecule, an electron-rich region was identified surrounding the pyridine ring, benzene ring, and methyl group, carbon

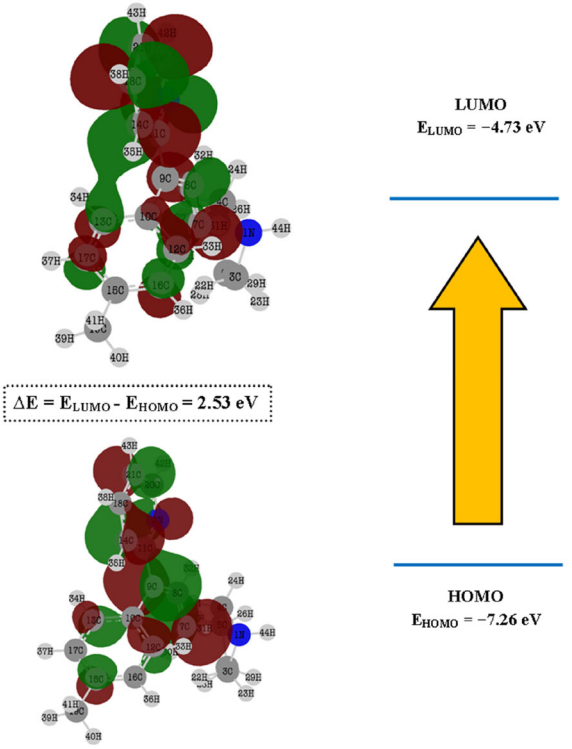

Figure 3. FMOs of Triprolidine.

Table 3. The calculated FMOs related molecular properties of the Triprolidine (Compound ID:5282443) molecule.

Molecular properties	Energy (eV)
E_{HOMO}	−7.26
E_{LUMO}	−4.73
Energy gap	2.53
Ionization energy (I)	7.26
Electron Affinity (A)	4.73
Global hardness (η)	1.27
Global Softness (S)	0.79
Chemical potential (μ)	−5.99
Electrophilicity index (ψ)	14.12

atom, indicating that charge transfer from the pyridine ring nitrogen atom N2 and carbon atom C14 to the methyl group carbon atom C19. The molecule's slightly electron-deficient (light blue) region was observed for all hydrogen atoms. The molecule's region around hydrogen atom H44 was electron-deficient (blue). Over the molecule, the neutral electrostatic potential envelopes (green) were projected. As a result of the MEP analysis, the hydrogen atom H44 and the pyridine ring nitrogen atom N2 are potential electrophilic and nucleophilic attack sites, respectively.

3.6. Mulliken atomic charge distribution analysis

Mulliken atomic charge distribution influence on dipole moment of a molecule, polarizability, electronic structure, vibrational modes, electrostatic potential model outside the molecular surface, and process of electronegativity equalization.[37] The computed Mulliken atomic charge distribution values for the molecule are listed in Table 5. Table 5 shows that the carbon atom C14

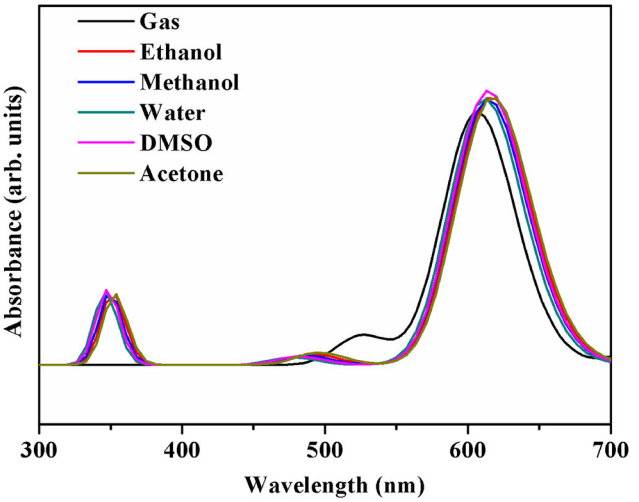

Figure 4. The simulated UV-visible spectra of Triprolidine in the gas phase and various solvents.

Table 4. The calculated absorption wavelength λ (nm), excitation energy values E (eV), oscillator strength (f), and orbital contributions for Triprolidine (Compound ID:5282443) molecule with its assignments.

Solvents	λ (nm)	E (eV)	f	Orbital contributions	Assignments
Gas	–	–	–	–	–
	607	2.0428	0.0784	H→L + 4 (91%)	n→ π^*
Water	346	3.5806	0.0230	H→L + 5 (95%)	π→ π^*
	612	2.0262	0.0825	H→L + 3 (96%)	n→ π^*
Methanol	350	3.5471	0.0022	H→L + 5 (96%)	π→ π^*
	614	2.0195	0.0824	H→L + 3 (96%)	n→ π^*
DMSO	348	3.5639	0.0234	H→L + 5 (95%)	π→ π^*
	615	2.0178	0.0850	H→L + 3 (96%)	n→ π^*
Ethanol	351	3.5291	0.0223	H→L + 5 (96%)	π→ π^*
	616	2.0119	0.0833	H→L + 3 (96%)	n→ π^*
Acetone	353	3.5133	0.0221	H→L + 5 (96%)	π→ π^*
	618	2.0077	0.0831	H→L + 3 (95%)	n→ π^*

(0.4208) of the pyridine ring and the carbon atom C19 (−0.7324) of the methyl group have larger positive and negative charge values. The delocalization of electrons within the molecule is confirmed by the higher negative charge value of the carbon atom.

The molecule's Mulliken atomic charge distribution shows that all hydrogen atoms have positive charge values, while nitrogen atoms have negative charge values. However, carbon atoms have both positive and negative charge values, so their substituents dominate carbon atoms. Because of the electronegative nitrogen atom N1 attached to this hydrogen atom, H44 has a higher positive charge value (0.3209) than other hydrogen atoms. According to the Mulliken atomic charge distribution analysis, the pyridine ring and a methyl group or hydrogen atom H44 are possible sites for electrophilic and nucleophilic attack. The MEP surface analysis is validated as a result of this result.

3.7. Molecular docking

Computational Biology and bioinformatics-based designing of drug molecules consider molecular docking as a foremost utensil in discovery novel drug molecules.[38] The binding site residues of 3CLPro (4YOI) are Cys_145 and His_41, for RdRp (7BTF), the catalytic residues such as Asp_618,760,761 and for ACE2 (6M17), Lys_31 and Lys_353 actively involved in the binding site;

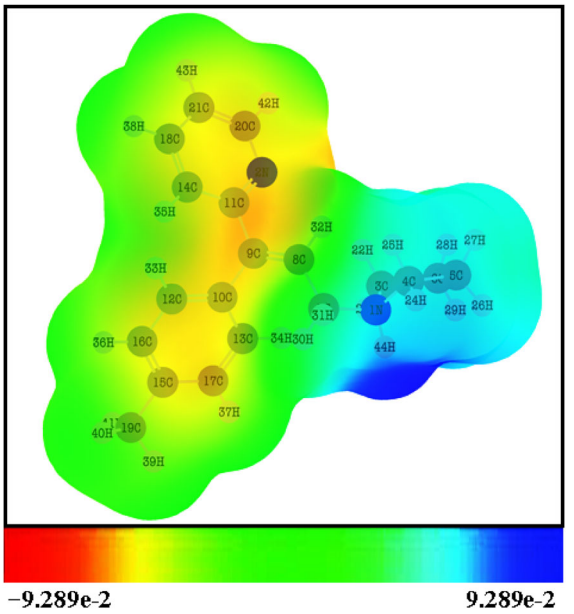

Figure 5. MEP surface of the Triprolidine.

Table 5. The calculated Mulliken atomic charge distribution of the Triprolidine (Compound ID:5282443) molecule.

Atom	Charge value	Atom	Charge value	Atom	Charge value	Atom	Charge value
N1	−0.3567	C12	−0.3706	H23	0.1445	H34	0.1479
N2	−0.0603	C13	−0.2183	H24	0.1377	H35	0.1469
C3	−0.2396	C14	0.4208	H25	0.1769	H36	0.1218
C4	−0.2485	C15	−0.0059	H26	0.1531	H37	0.1204
C5	−0.3517	C16	0.0323	H27	0.1525	H38	0.1239
C6	−0.3603	C17	0.1734	H28	0.1499	H39	0.1614
C7	−0.4021	C18	−0.5678	H29	0.1514	H40	0.1605
C8	0.1828	C19	−0.7324	H30	0.1329	H41	0.1716
C9	0.0017	C20	−0.0579	H31	0.1627	H42	0.1408
C10	−0.1604	C21	0.0789	H32	0.2135	H43	0.1337
C11	−0.4114	H22	0.1666	H33	0.1625	H44	0.3209

Nsp10 (6W4H), residues such as LYS4281, LEU4365 are acts as the binding sites. The Protein-Ligand (lead phytocompounds from *Elettaria cardamomum*) complex (4YOI_5282443) showed the docking score of about −8.20 Kcal/Mol and the interacting residues noted as Glu_169. Another complex 6M17_8748 showed the docking score of about −5.34 Kcal/Mol, and the interaction residues noted as Leu_52 and 6W4H_135 had the docking score of about −5.075 Kcal/Mol, and the interacting residues were Tyr_6930, Cys_6913, 7BTF_14985 showed the docking score of about −5.639 Kcal/Mol and the observed interacting residues was Thr_51, respectively (Table 6 and Figure 6). The docked lead complexes posses hydrogen bond interactions, which favored for the binding efficacy of the ligands. Lowest energy possessed the highest efficacy and binding free energy.

3.8. Binding free energy calculation

Binding free energy was performed for the different target proteins and the lead phytocompounds from *Elettaria cardamomum*. 4YOI_5282443 complex showed binding energy of about −36.85 KJ/

Table 6. Docking analysis of target proteins and phytocompounds from *Elettaria cardamomum*.

PDB ID and Compound ID	Docking score (Kcal/Mol)	Interaction residues	Binding energy (KJ/Mol)
4YOI_5282443	−8.20	Glu_169	−36.85
6M17_8748	−5.34	Leu_52	−32.603
6W4H_135	−5.075	Tyr_6930, Cys_6913	−31.093
7BTF_14985	−5.639	Thr_51	−30.117

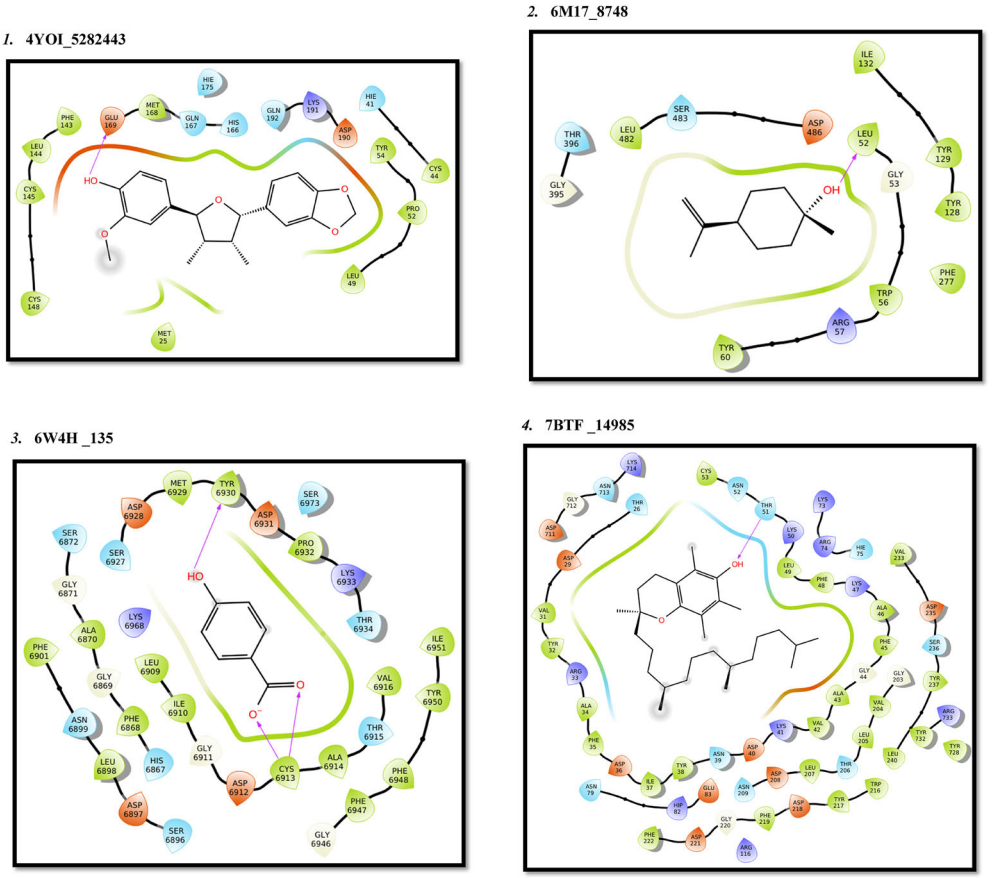

Figure 6. Molecular docking analysis of target protein and the lead compounds from *Elettaria cardamomum*.

Mol. The 6M17_8748 complex had an energy of about −32.603 KJ/Mol; 6W4H_135 showed the binding energy of about −31.093 KJ/Mol; 7BTF_14985 showed the binding energy of about −30.117 KJ/Mol, respectively (Table 6).

3.9. ADME prediction

ADME studies help find out the pharmacological properties of the phytocompounds. The results concluded that the phytocompounds had adequate Human oral absorption, hydrogen bond donor and acceptor, octanol in water, molecular weight, and also it supports Lipinski's rule of five (Table 7). A molecule's ADME characteristics are a key predictor of its medicinal efficacy. The drug similarity of novel drug compounds is influenced by the ADME and bioavailability tests. Moreover, the pharmacokinetic analysis (drug likeliness test) performed on the lead compounds

Table 7. ADME properties of the phytocompounds from *Elettaria cardamomum*.

Compound ID	Mol.Wt	HB Donor	HB Acceptor	QPlogPo/w	HOA (%)	QPPMDCK	QPPCaco
5282443	278.31	0.000	3.000	4.267	100	1044.3	1818.0
135	138.123	2.000	2.750	0.578	64.10	39.410	77.072
8748	154.23	1.000	0.750	2.916	100	865.193	890.53
14985	430.71	1.000	1.500	2.167	100	2566.6	4586.9

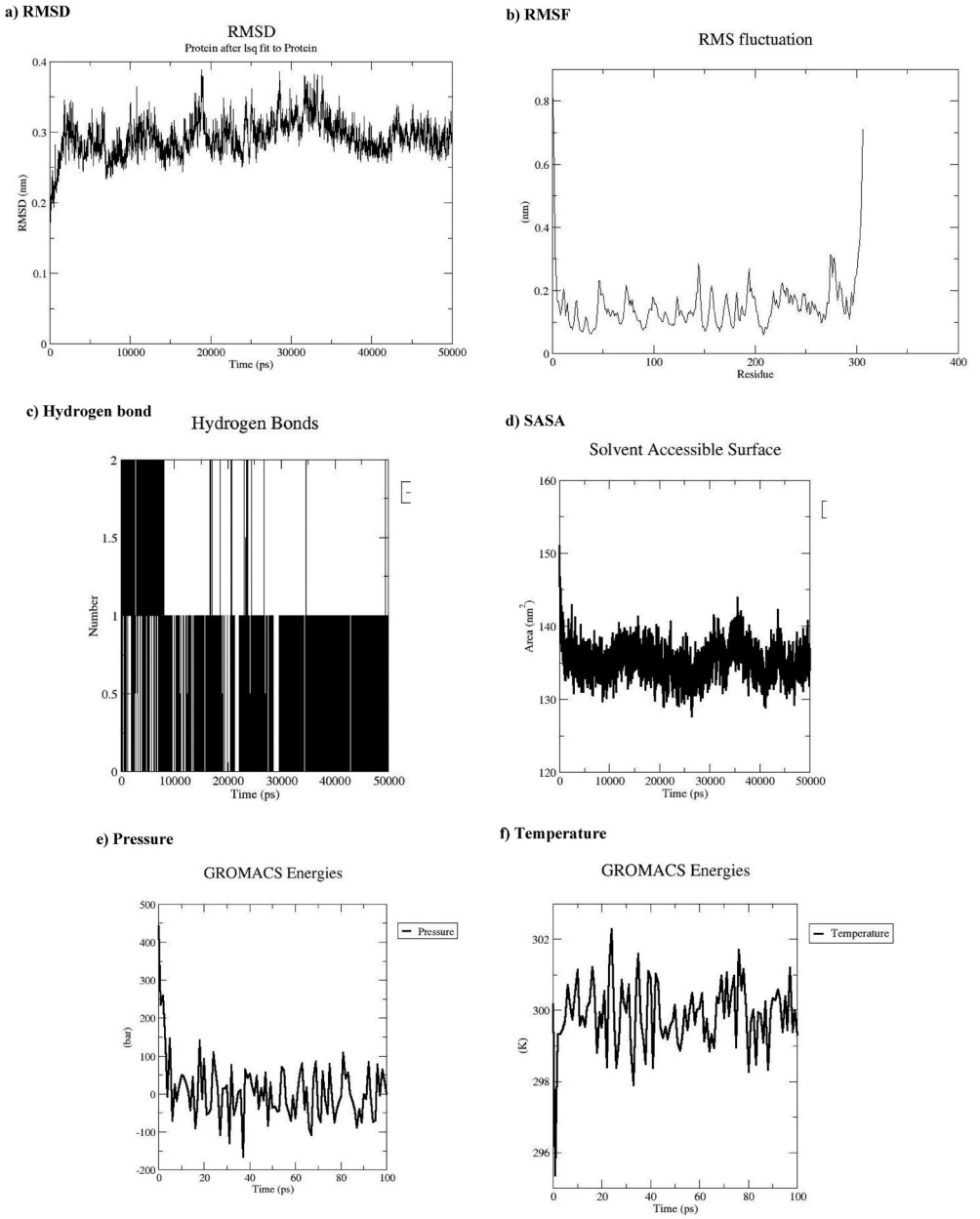

Figure 7. Molecular dynamics simulation of the complexes, 4YOI-*Elettaria cardamomum* (5282443).

indicated that all of the compounds passed the drug likeness test (ADME and other physicochemical properties) and had no violations to the Lipinski rule of five, which is a standard measure for evaluating the drug likeness of molecules.

3.10. Molecular dynamics simulation

Molecular Dynamics (MD) simulation research was done to confirm the stability of the projected docked complexes. The root mean square deviation (RMSD) and root mean square fluctuation (RMSF) plots were used to analyze the findings of MD trajectories, which might give important insights into comprehending structural changes in atomic details. The RMSD is an important measure for analyzing equilibrium in MD trajectories, and it is calculated for protein and ligand complex backbone atoms. The simulation was used to look at RMSD, RMSF, and the hydrogen bond for a period of 50 ns. There was a minimum RMSD devitation for the protein with 4YOI-5282443 complexes during the simulation with an RMSD of 0.35–0.37 nm. Within the limit of 0.3 nm the RMSF value of complexes for each residue occurs. 0 to 6 ns with RMSD of 0.13 to 0.2 nm the complex deviated and remained stable from 6 to 16 ns. The most significant, three H-bonds were preserved during the simulation, illustrating the importance of protein stability within the binding cavity. SASA may theoretically be used to define the protein solvent interactions ratio, which estimates the degree of conformational changes in binding processes and can be used to assess the accessibility of protein. The SASA (Solvent Accessible Surface Area) of the complex fluctuated at the range of 140 nm with the slightest oscillation during the simulation, it doesn't affect the stability and make the complex compact. The temperature and pressure were manintained at 300 K. The resultant plotes were displayed (Figure 7).

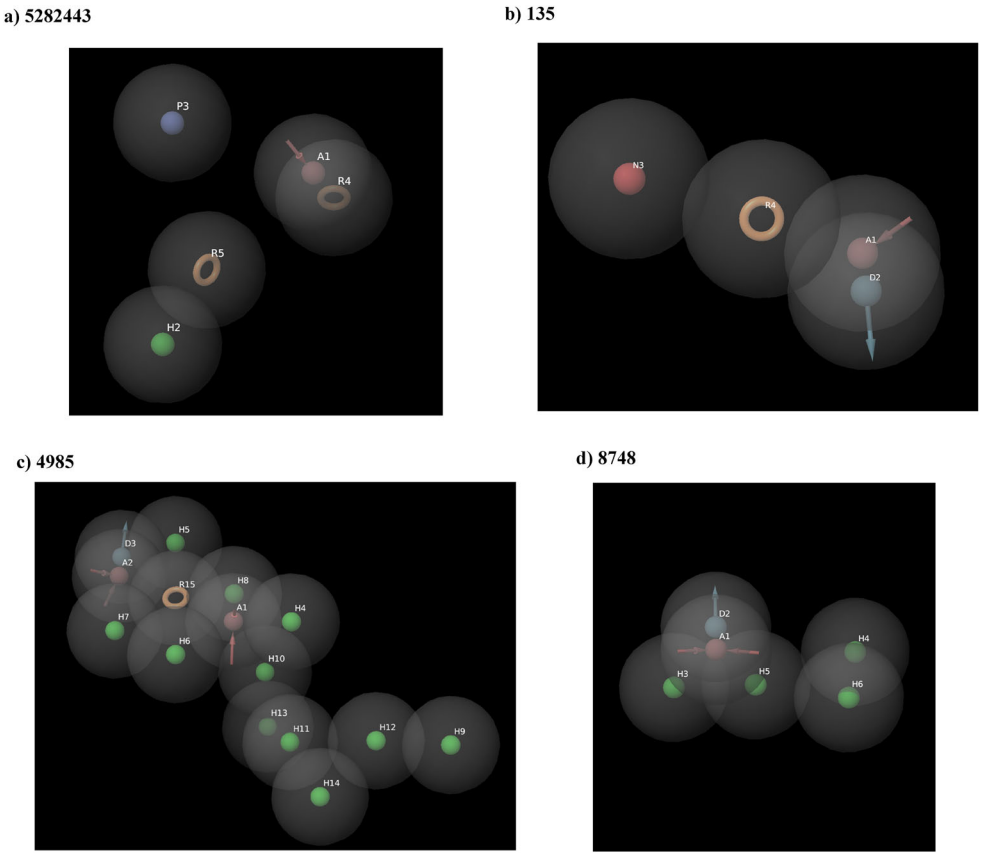

Figure 8. Pharmacophore model of the lead.

3.11. Pharmacophore features

Pharamacophoreic features of the lead compound (5282443) were illustrated in Figure 8.

4. Conclusion

The quantum chemical investigations, molecular docking, and molecular dynamics simulation studies of Triprolidine molecule were performed. The most stable molecular structure of the title molecule was optimized, and structural parameters including the bond length, bond angle, and dihedral angle values of the molecule were calculated. FMOs study reveals that the title molecule has a low energy gap value, indicating that the molecule has an intramolecular charge-transfer interaction. The effect of the solvent on UV-Visible spectra and the molecule's electronic transitions were predicted. The electrophilic and nucleophilic attack sites in the molecule are confirmed by MEP surface and Mulliken atomic charge distribution investigations. The study concluded that the phytocompound Triprolidine from *Elettaria cardamomum* had the better docking and binding affinities to the various Covid target proteins. Also, it obeyed all the pharmacological relevant properties. Phytocompound Triprolidine showed better stability and lesser fluctuation through Molecular Dynamics simulation.

Disclosure statement

The authors reported no potential conflict of interest

Funding

The authors thankfully acknowledge MHRD-RUSA 2.0 [F.24/51/2014-U, Policy (TN Multi-Gen), Dept. of Edn. Govt. of India], the financial grant supported by DST–FIST (SR/FST/LSI-667/2016) (C), and Department of Bioinformatics, Alagappa University for the financial supports and infrastructure facilities.

References

1. Z. Zhou, Y. Qiu, and X. Ge, "The Taxonomy, Host Range, and Pathogenicity of Coronaviruses and Other Viruses in the Nidovirales Order," *Animal Diseases* 1, no. 1 (2021): 5. doi:10.1186/s44149-021-00005-9.
2. M. Pal, G. Berhanu, C. Desalegn, and V. Kandi, "Severe Acute Respiratory Syndrome Coronavirus-2 (SARS-CoV-2): An Update," *Cureus* 12, no. 3 (2020): e7423. doi:10.7759/cureus.7423.
3. M. Jayaweera, H. Perera, B. Gunawardana, and J. Manatunge, "Transmission of COVID-19 Virus by Droplets and Aerosols: A Critical Review on the Unresolved Dichotomy," *Environmental Research* 188 (2020): 109819. (2020).109819. doi:10.1016/j.envres.
4. A. Alam, T. Jawaid, and P. Alam, "In Vitro Antioxidant and anti-Inflammatory Activities of Green Cardamom Essential Oil and in Silico Molecular Docking of Its Major Bioactives," *Journal of Taibah University for Science* 15, no. 1 (2021): 757–68. doi:10.1080/16583655.2021.2002550.
5. G. M. N. Bhat, N. Nayak, K. Vinodraj, N. Chandralekha, P. Mathai, and J. Cherian, "Comparison of the Efficacy of Cardamom (*Elettaria cardamomum*) with Pioglitazone on Dexamethasone-Induced Hepatic Steatosis, Dyslipidemia, and Hyperglycemia in Albino Rats," *Journal of Advanced Pharmaceutical Technology & Research* 6, no. 3 (2015): 136. doi:10.4103/2231-4040.157981.
6. K. Ashokkumar, M. Murugan, M. K. Dhanya, S. Raj, and D. Kamaraj, "Phytochemical Variations among Four Distinct Varieties of Indian Cardamom *Elettaria cardamomum* (L.) Maton," *Natural Product Research* 34, no. 13 (2020): 1919–22. doi:10.1080/14786419.2018.1561687.
7. W. Cui, A. Aouidate, S. Wang, Q. Yu, Y. Li, and S. Yuan, "Discovering Anti-Cancer Drugs *via* Computational Methods," *Frontiers in Pharmacology* 11 (2020): 733. doi:10.3389/fphar.2020.00733.
8. R. Premkumar, S. Hussain, N. D. Jayram, S.-J. Koyambo-Konzapa, M. S. Revathy, T. Mathavan, and A. Milton Franklin Benial, "Adsorption and Orientation Characteristics of 1-Methylpyrrole-2-Carbonyl

Chloride Using SERS and DFT Investigations," *Journal of Molecular Structure* 1253 (2022): 132201. doi:10.1016/j.molstruc.2021.132201.
9. S.-J. Koyambo-Konzapa, R. Premkumar, R. V. Berthelot Saïd Duvalier, M. K. Gilbert Yvon, M. Nsangou, and A. M. F. Benial, "Electronic, Spectroscopic, Molecular Docking and Molecular Dynamics Studies of Neutral and Zwitterionic Forms of 3, 4-dihydroxy-L-Phenylalanine: A Novel Lung Cancer Drug," *Journal of Molecular Structure* 1260 (2022): 132844. doi:10.1016/j.molstruc.2022.132844.
10. M. J. Frisch, G. W. Trucks, H. B. Schlegel, G. E. Scuseria, M. A. Robb, J. R. Cheeseman, G. Scalmani, V. Barone, B. Mennucci, G. A. Petersson, et al., *Gaussian 09, Revision C. 02* (Wallingford, CT: Gaussian Inc., 2009).
11. R. Dennington, T. Keith, and J. Milam, *Gauss View, Version 5* (Shawnee Mission, KS: Semichem Inc., 2009).
12. *Schrödinger Release 2019-4* (New York: Schrödinger, LLC, 2019).
13. P. Sangavi and K. Langeswaran, "Anti-Tumorigenic Efficacy of Tangeretin in Liver Cancer – An In Silico Approach," *Current Computer-Aided Drug Design* 17, no. 3 (2021): 337–43. doi:10.2174/1573409916666200219120254.
14. P. Sangavi and K. Langeswaran, "Identification of Potential Elephantiasis Inhibitors against UDP-Galactopyranose Mutase (UGM) Using Virtual Screening and Molecular Docking," *Journal of Current Enzyme Inhibition* 17, no. 1 (2021): 57–70.
15. C. Nayak and S. K. Singh, "In Silico Identification of Natural Product Inhibitors against Octamer-Binding Transcription Factor 4 (Oct4) to Impede the Mechanism of Glioma Stem Cells," *PLoS One* 16, no. 10 (2021): e0255803. doi:10.1371/journal.pone.0255803.
16. Schrödinger Release 2020–2, *QikProp* (New York, NY: Schrödinger, LLC, 2020).
17. K. Choubey Sanjay and J. Jeyaraman, "A Mechanistic Approach to Explore Novel HDAC1 Inhibitor Using Pharmacophore Modeling, 3D-QSAR Analysis, Molecular Docking, Density Functional and Molecular Dynamics Simulation Study," *Journal of Molecular Graphics & Modelling* 70 (2016): 54–69. doi:10.1016/j.jmgm.2016.09.008.
18. J. A. Lemkul, "From Proteins to Perturbed Hamiltonians: A Suite of Tutorials for the GROMACS-2018 Molecular Simulation Package, v1.0," *Living Journal of Computational Molecular Science* 1, no. 1 (2018): 5068.
19. T. Valarmathi, R. Premkumar, and A. M. Franklin Benial, "Spectroscopic and Molecular Docking Studies on 1-Hydroxyanthraquinone: A Potent Ovarian Cancer Drug," *Journal of Molecular Structure* 1213 (2020): 128163. doi:10.1016/j.molstruc.2020.128163.
20. T. Valarmathi, R. Premkumar, and A. M. Franklin Benial, "Quantum Chemical and Molecular Docking Studies on 1,4-Bis(Methylamino)Anthraquinone: A DFT Approach," *American Institute of Physics Conference Proceedings* 2270 (2020): 040001.
21. R. M. Asath, R. Premkumar, T. Mathavan, and A. M. Franklin Benial, "Structural, Spectroscopic and Molecular Docking Studies on 2-Amino-3-Chloro-5-Trifluoromethyl Pyridine: A Potential Bioactive Agent," *Spectrochimica Acta. Part A, Molecular and Biomolecular Spectroscopy* 175 (2017): 51–60. doi:10.1016/j.saa.2016.11.037.
22. G. Socrates, *Infrared and Raman Characteristic Group Frequencies*, 3rd ed. (New York: Wiley, 2001).
23. G. Varsanyi, *Assignments for Vibrational Spectra of Seven Hundred Benzene Derivatives*, Vol. I. (London: Adam Hilger, 1974).
24. L. J. Bellamy, *The Infra-Red Spectra of Complex Molecules* (New York: John Wiley and Sons, Inc., 1975).
25. M. Karabacak, D. Karagoz, and M. Kurt, "Experimental (FT-IR and FT-Raman Spectra) and Theoretical (Ab Initio HF, DFT) Study of 2-Chloro-5-Methylaniline," *Journal of Molecular Structure* 892, no. 1-3 (2008): 25–31. doi:10.1016/j.molstruc.2008.04.054.
26. J. F. Areans, I. Lopez, M. S. Wooley, J. C. Otero, J. I. Marcos, and J. Otero, "Vibrational Spectrum and Internal Rotation in 2-Methylpyrazine," *Journal of the Chemical Society, Faraday Transactions II* 84, no. 1 (1988): 53–65. doi:10.1039/F29888400053.
27. A. I. Almansour, N. Arumugam, S. M. Soliman, B. S. Krishnamoorthy, J.-F. Halet, R. V. Priya, J. Suresh, D. M. Al-Thamili, F. A. Al-Aizari, and R. S. Kumar, "Stereoselective Synthesis, Structure and DFT Studies on Fluoro- and Nitro- Substituted Spirooxindole-Pyrrolidine Heterocyclic Hybrids," *Journal of Molecular Structure* 1237 (2021): 130396. doi:10.1016/j.molstruc.2021.130396.
28. Z. Zhou, Y. Liu, Q. Ren, D. Yu, and H. Lu, "Synthesis, Crystal Structure and DFT Study of a Novel Compound *N*-(4-(2,4-Dimorpholinopyrido[2,3-*d*]Pyrimidin-6-yl)Phenyl)Pyrrolidine-1-Carboxamide," *Journal of Molecular Structure* 1235 (2021): 130261. doi:10.1016/j.molstruc.2021.130261.
29. R. Premkumar, S. Hussain, S.-J. Koyambo-Konzapa, N. D. Jayram, M. R. Meera, T. Mathavan, and A. M. Franklin Benial, "SERS and DFT Studies of 2-(Trichloroacetyl)Pyrrole Chemisorbed on the Surface of Silver and Gold Coated Thin Films: In Perspective of Biosensor Applications," *Journal of Molecular Recognition* 34, no. 11 (2021): e2921.

30. S. J. Koyambo-Konzapa, G. Y. Mbesse Kongbonga, R. Premkumar, B. S. Duvalier Ramlina Vamhindi, M. Nsangou, and A. M. Franklin Benial, "Spectroscopic, Quantum Chemical, Molecular Docking and Molecular Dynamics Investigations of Hydroxylic Indole-3-Pyruvic Acid: A Potent Candidate for Nonlinear Optical Applications and Alzheimer's Drug," *Journal of Biomolecular Structure and Dynamics* (2021): 1–14. doi:10.1080/07391102.2021.1947380.
31. B. Babu, J. Chandrasekaran, B. Mohanbabu, Y. Matsushita, and M. Saravanakumar, "Growth, Physicochemical and Quantum Chemical Investigations on 2-Amino 5-Chloropyridinium 4-Carboxybutanoate-an Organic Crystal for Biological and Optoelectronic Device Applications," *RSC Advances* 6, no. 112 (2016): 110884–97. doi:10.1039/C6RA15791B.
32. R. Mohamed Asath, R. Premkumar, T. Mathavan, and A. M. Franklin Benial, "Spectroscopic and Molecular Docking Studies on N,N-di-Tert-Butoxycarbonyl (Boc)-2-Amino Pyridine: A Potential Bioactive Agent for Lung Cancer Treatment," *Journal of Molecular Structure.* 1143 (2017): 415–23. doi:10.1016/j.molstruc.2017.04.117.
33. R. Premkumar, S. Hussain, S.-J. Koyambo-Konzapa, N. Dhanpal Jayram, T. Mathavan, and A. M. Franklin Benial, "SERS and DFT Investigations of Methyl 4-Bromo-1H-Pyrrole-2-Carboxylate Adsorbed on Silver and Gold Substrates: In Perspective of Biosensor Applications," *Journal of Molecular Structure* 1236 (2021): 130272. doi:10.1016/j.molstruc.2021.130272.
34. L. R. Domingo, M. Ríos-Gutiérrez, and P. Pérez, "Applications of the Conceptual Density Functional Theory Indices to Organic Chemistry Reactivity," *Molecules* 21, no. 6 (2016): 748. doi:10.3390/molecules21060748.
35. S. Saravanan and V. Balachandran, "Quantum Mechanical Study and Spectroscopic (FT-IR, FT-Raman, UV–Visible) Study, Potential Energy Surface Scan, Fukui Function Analysis and HOMO–LUMO Analysis of 3-Tert-Butyl-4-Methoxyphenol by DFT Methods," *Spectrochimica Acta. Part A, Molecular and Biomolecular Spectroscopy* 130 (2014): 604–20.
36. T. Valarmathi, R. Premkumar, M. R. Meera, and A. M. Franklin Benial, "Spectroscopic, Quantum Chemical and Molecular Docking Studies on 1-Amino-5-Chloroanthraquinone: A Targeted Drug Therapy for Thyroid Cancer," *Spectrochimica Acta. Part A, Molecular and Biomolecular Spectroscopy* 255, no. 3 (2021): 119659.
37. G. Pandimeena, R. Premkumar, T. Mathavan, and A. M. Franklin Benial, "Spectroscopic, Quantum Chemical and Molecular Docking Studies on Methyl 6-Aminopyridine-3-Carboxylate: A Potent Bioactive Agent for the Treatment of Sarcoidosis," *Journal of Molecular Structure* 1231 (2021): 129996. doi:10.1016/j.molstruc.2021.129996.
38. R. Geetha, M. R. Meera, C. Vijayakumar, R. Premkumar, and A. M. Franklin Benial, "Synthesis, Spectroscopic Characterization, Molecular Docking and in Vitro Cytotoxicity Investigations on 8-Amino-6-Methoxy Quinolinium Picrate: A Novel Breast Cancer Drug," *Journal of Biomolecular Structure and Dynamics* (2021). doi:10.1080/07391102.2021.2024259.